Geophysical Research Letters

RESEARCH LETTER
10.1029/2024GL112814

Propagation and Periodicity of Mars's Northern Annular Mode Modulates the Dust Cycle

J. Michael Battalio[1], Juan M. Lora[1], Sandro W. Lubis[2], and Pedram Hassanzadeh[3]

[1]Department of Earth and Planetary Sciences, Yale University, New Haven, CT, USA, [2]Pacific Northwest National Laboratory Richland, Richland, WA, USA, [3]Department of the Geophysical Sciences, University of Chicago, Chicago, IL, USA

Key Points:

- Mars's Northern Annular Mode (MNAM), diagnosed from a reanalysis dataset, propagates with a 150-day period, independent of the season
- Like Earth's, MNAM arises from feedbacks between the two leading empirical orthogonal functions of anomalous zonal-mean zonal wind
- Surface wind stress and dust opacity vary with a matching 150-day period, suggesting that the MNAM imparts variability on large dust storms

Supporting Information:

Supporting Information may be found in the online version of this article.

Correspondence to:

J. M. Battalio,
michael@battalio.com

Citation:

Battalio, J. M., Lora, J. M., Lubis, S. W., & Hassanzadeh, P. (2025). Propagation and periodicity of Mars's Northern Annular Mode modulates the dust cycle. *Geophysical Research Letters*, *52*, e2024GL112814. https://doi.org/10.1029/2024GL112814

Received 27 SEP 2024
Accepted 18 FEB 2025

Author Contributions:

Conceptualization: J. Michael Battalio, Juan M. Lora, Sandro W. Lubis, Pedram Hassanzadeh
Formal analysis: J. Michael Battalio
Funding acquisition: J. Michael Battalio
Investigation: J. Michael Battalio
Methodology: J. Michael Battalio, Juan M. Lora, Sandro W. Lubis, Pedram Hassanzadeh
Project administration: J. Michael Battalio
Software: J. Michael Battalio
Validation: J. Michael Battalio
Visualization: J. Michael Battalio
Writing – original draft: J. Michael Battalio

Abstract We document the propagation of annular modes—zonally symmetric patterns of variability—in Mars's atmosphere using a reanalysis dataset. Mars's Northern Annular Mode (MNAM) sees anomalies of zonal-mean zonal wind emerge near the subtropics and migrate poleward with a period of ∼150 days, similarly to Earth's Southern Annular Mode. The mechanism of propagation involves the interaction of the two leading empirical orthogonal functions that define the MNAM. Moreover, the propagation encourages alternating bands of surface wind stress to migrate polewards with a 150-day period. In addition, a 150-day periodicity in anomalous column dust optical depth most likely emerges in response to extrema of the MNAM. The combination of the impact of the MNAM's internally forced periodicity on the surface wind stress and the seasonal cycle may contribute to the inter-annual variability of global dust events, as suggested by a Monte Carlo estimate that correctly approximates the observed incidence of global dust events.

Plain Language Summary Some of the largest sources of climate variability for Earth and Mars are annular modes. These phenomena represent shifts of the jet stream north and south in time, and are related to atmospheric eddies, clouds, and/or dust (depending on the planet). Earth's Southern Hemisphere annular mode migrates with time from lower latitudes toward the pole every 150 days, and this timing has previously been shown to be related to precipitation patterns. Remarkably, we find that Mars's Northern Hemisphere annular mode similarly migrates poleward with a 150 Mars-day period. The mechanism controlling this timing stems from different types of patterns of variability interacting with themselves and one another, which can be predicted using a pair of simple prognostic equations. Mars's annular mode relates to surface wind stress that contributes to dust lifting and the amount of dust in the atmosphere, which both exhibit the same ∼150 Mars-day periodicity. This period, which is not related to the seasonal cycle, may contribute to the large differences in the timing of global dust events in different Mars years.

1. Introduction

Annular modes define the largest known source of hemisphere-scale variability at seasonal to sub-seasonal timescales in the midlatitudes of Earth (Kidson, 1988; Lorenz & Hartmann, 2001; D. W. Thompson & Wallace, 2000) and Mars (Battalio & Lora, 2021). Earth has Northern (NAM) and Southern Annular Modes (SAM) that describe meridional fluctuations of each hemisphere's zonal-mean jet stream. The NAM/SAM are generally quantified as the leading empirical orthogonal function (EOF1) from daily anomalies of the zonal-mean zonal wind (Hannachi et al., 2007; Hartmann & Lo, 1998; D. W. J. Thompson & Barnes, 2014; D. W. Thompson & Wallace, 2000). The state of the NAM/SAM impacts the weather and climate regimes, including atmospheric composition, clouds, precipitation, and temperatures (Butler et al., 2007; Doddridge & Marshall, 2017; Eabry et al., 2024; Hell et al., 2021; Marshall et al., 2017, 2018). The second leading EOF (EOF2) of zonal-mean zonal wind anomalies is implicated in the propagation of the jet and its associated climate impacts poleward (Lubis & Hassanzadeh, 2023).

Poleward propagation of jet winds on Earth has been observed in both hemispheres (S. S. Feldstein & Lee, 1998; Son & Lee, 2006; Sheshadri & Plumb, 2017), and the propagation of the observed annular mode has recently been demonstrated (Lubis & Hassanzadeh, 2021, 2023). Propagation of the annular mode results from the feedback of anomalous transient eddy momentum fluxes generated by EOF1 onto the zonal-mean wind associated with EOF2 and eddy momentum fluxes generated by EOF2 onto the zonal-mean wind associated with EOF1. Because the EOFs have centers of action offset in latitude from one another, the feedback of the modes forces a drift of their

Writing – review & editing:
J. Michael Battalio, Juan M. Lora, Sandro W. Lubis, Pedram Hassanzadeh

spatial structures toward the pole. Over many days, the structure of EOF1 comes to resemble EOF2, and vice versa, so that the propagation repeats with an internally set period (S. S. Feldstein & Lee, 1998; Son & Lee, 2006; Sheshadri & Plumb, 2017). On Earth, propagation is observed in the spectrum of the first principal component with a ∼150 day period, which is predictable with a reduced-order model (Lubis & Hassanzadeh, 2021, 2023).

Mars's NAM (MNAM) shares many similarities with Earth's SAM, with a dipole structure signaling the equatorward or poleward phases of the mode (D. W. J. Thompson & Barnes, 2014; Battalio & Lora, 2021). The MNAM explains upwards of 50% of the variance in the zonal wind, with an associated principal component time series that follows red noise (Battalio et al., 2025), like the SAM (S. B. Feldstein, 2000; Lorenz & Hartmann, 2001; Ma et al., 2017). A natural question, addressed here, is whether the MNAM also propagates poleward. In addition to advancing understanding of Mars's atmospheric dynamics, characterizing annular mode propagation could have important implications for the timing of Mars's dust storms. Generally, the timing of regional dust events is confined within seasonal windows, but the size and progression of dust events experiences considerable year-to-year modulation (Battalio & Wang, 2021; Kass et al., 2016; Montabone, Spiga, et al., 2020). The most prominent variability is the irregular development of global dust events (Battalio et al., 2023; Wang et al., 2023; Wolkenberg et al., 2020) that can occur more than once a year or only once in several Mars years. Multiple theories have been advanced to account for this variability, including orbit-spin coupling (Shirley, 2015; Shirley et al., 2020) or redistribution of dust sources (Kahre et al., 2005; Newman & Richardson, 2015), but the processes underlying the irregular return interval remain unclear. The state of the annular modes has been linked to the occurrence of dust storms (Battalio & Lora, 2021), which suggests the possibility of annular modes for their variability.

2. Methods

We investigate annular mode propagation on Mars using the Open access to Mars Assimilated Remote Soundings (OpenMARS v1.0) (Holmes et al., 2020) reanalysis for Mars Years (MY) 29–35. We generate a yearly climatology of daily winds to define the anomalies (see Text S1 in Supporting Information S1) to investigate annular modes. We also investigate the effect of annular mode propagation on column dust optical depth (CDOD) at 9.3 μm (scaled to a surface pressure of 610 Pa) (Montabone et al., 2015; Montabone, Spiga, et al., 2020). We use the spatially interpolated and kriged daily CDOD maps to generate climatological anomalies from MY 29–35 for comparison to the annular modes.

An important distinction in our methodology from the quantification of annular mode dynamics for Earth stems from the intermittent global and regional dust events that impact the atmospheric dynamics and global circulation (Battalio et al., 2023; Battalio & Wang, 2021; Montabone et al., 2015; Montabone, Spiga, et al., 2020; Wang et al., 2023). This variability complicates the analysis of internal mode propagation. We calculate the EOFs only for periods without a global dust event on Mars; that is, ignoring MY 28 entirely and L_s = 180–360° of MY 34. We exclude the global event years because only two events would impart spectral power at half the length of the reanalysis length. Including spectral power at 0.25 yr^{-1} in only eight Mars years of OpenMARS would be artificial, given the variability of global dust events in the observed record (Shirley et al., 2020). In addition, we compare the calculation of EOFs between the full years and on the fall to winter seasons only for both hemispheres (L_s = 350–190° for the southern hemisphere and L_s = 170–10° for the northern hemisphere).

We follow the methods of Simpson et al. (2013) and Lubis and Hassanzadeh (2021); Lubis and Hassanzadeh (2023) to define the EOFs of the zonal wind, the forcing of the EOFs by the eddies, and the zonal indices of EOFs and forcing. The EOFs are first calculated in each hemisphere on data linearly interpolated to 1° latitudinal resolution between 25° and 85° N/S and 550–50 Pa. The interpolation does not statistically impact the native EOF calculations. Extending the domain closer to the equator does not appreciably change the EOF structures in the midlatitudes and polar region, nor does changing the height alter the EOFs (Battalio & Lora, 2021). EOFs are calculated from the climatologically anomalous ($\bar{\cdot}$), zonal-mean ($[\cdot]$), vertically averaged ($\langle\cdot\rangle$) zonal winds $\langle[\overline{u}]\rangle$ weighted by the square root of the cosine of latitude (Chung & Nigam, 1999) and the square root of the mass of atmosphere represented in each pressure level. The zonal indices (z_1 and z_2) corresponding to the first two leading EOFs of $\langle[\overline{u}]\rangle$ (EOF1 and EOF2) are generated by projecting the EOFs back onto $\langle[\overline{u}]\rangle$. The time series of the eddy forcing (m_1 and m_2) are found by projecting EOF1 and EOF2 onto the vertically averaged, zonal-mean anomalies of eddy momentum flux convergence $\langle[\overline{F}]\rangle$ (Lorenz & Hartmann, 2001; Lubis & Hassanzadeh, 2021, 2023; Simpson et al., 2013):

$$z_j(t) = \frac{\langle [\mathbf{u}] \rangle (t) \mathbf{W} \mathbf{e_j}}{\sqrt{\mathbf{e_j^T} \mathbf{W} \mathbf{e_j}}} \quad (1)$$

$$m_j(t) = \frac{\langle [\mathbf{F}] \rangle (t) \mathbf{W} \mathbf{e_j}}{\sqrt{\mathbf{e_j^T} \mathbf{W} \mathbf{e_j}}}, \quad (2)$$

where $j = 1,2$, $\mathbf{e_j}$ is the jth EOF, $\mathbf{e_j^T}$ is its transpose, and $\mathbf{W}$ is the diagonal matrix with elements of cos ϕ along the diagonal. $\langle [F] \rangle$ is calculated in spherical coordinates:

$$\langle [\mathbf{F}] \rangle (t) = \langle [F] \rangle (t, \phi) = -\frac{1}{\cos^2 \phi} \frac{\partial \langle u^* v^* \cos^2 \phi \rangle}{a \partial \phi}, \quad (3)$$

where starred variables indicate deviations from the zonal mean, ϕ is latitude, and $a = 3{,}390$ km is Mars's radius. Correlation maps showing the lead-lag behavior of winds are generated from the vertical average from 550 to 50 Pa to remain above the highest topography in the southern hemisphere and within Mars's troposphere. Correlation significance is assessed with the Bartlett test (Lubis & Hassanzadeh, 2023).

Annular mode propagation is an internal process to the eddy-driven jet (Lu et al., 2024; Lubis & Hassanzadeh, 2021, 2023), so any external forcing would obscure its diagnosis. On Mars, the short radiative timescale and smaller planetary radius contribute to large swings in the ascending and descending branches of the Hadley circulation (Barnes et al., 2017; Guendelman & Kaspi, 2022; Williams et al., 2024). The variation of the general circulation changes the location of the subtropical, angular momentum-conserving jet (Read et al., 2015), which externally imparts propagation on $\langle [\bar{u}] \rangle$ at seasonal timescales. We repeat the calculation of EOFs after this effect is removed by subtracting the seasonal cycle of the edge of the Hadley circulation. To remove the seasonal cycle, we calculate the location of the climatological maximum in the westerly jet stream separately for each hemisphere (solid line Figure S1a in Supporting Information S1) and shift the location of the zonal winds in latitude so that every timestep has the maximum jet at the same latitude (Figure 1b in Supporting Information S1). We refer to EOFs calculated on this as "jet-shifted," and we also use this to coordinate shift all variables in latitude. The cosine of latitude weightings are applied before the coordinate-shift, but applying them after the coordinate shift does not appreciably change the conclusions.

3. Results

The MNAM and MSAM are as robust in OpenMARS (Figure 1) as they are in earlier reanalyzes (Battalio & Lora, 2021). In both hemispheres, EOF1 of zonal-mean zonal wind is dipolar and explains over 50% of the variance; EOF2 is tripolar and explains 20–25% of the variance. The EOFs calculated from the fall–winter seasons (Figures 1a, 1b, 1d, 1e, 1g and 1h shading) are nearly identical to the EOFs calculated from the whole year (Figures 1a, 1b, 1d, 1e, 1g, and 1h contours). The edges of the centers of action are shifted somewhat toward the equator compared to the whole-year EOFs, especially for the jet-shifted cases (Figures 1d, 1e, 1g, and 1h contours). For example, the jet-shifted EOF1 has a third, positive pole of action along −30° relative latitude for the fall–winter year (Figure 1d shading), while the negative pole for the whole-year EOF1 extends beyond −30° relative latitude (Figure 1d contours). Regardless, the location of the centers of the poles of action and their vertical structures match. The jet-shifted MNAM is similar in structure to the native-latitude MNAM, with poles at ±15° relative latitude (Figure 1d). Both the latitude-native and jet-shifted EOF1 are similar, meaning that the seasonal cycle does not overly influence the jet shifts. The northernmost MNAM EOF2 has a stronger center of action in the jet-shifted coordinate, which signifies that the seasonal cycle masks the northern sharpening of the jet that EOF2 is generally interpreted to represent. However, the eigenvalues of the jet-shifted EOF1 and EOF2 (quantified in Figure 1 as the percentage of variance explained) have values closer together versus the native latitude versions. The jet-shifted EOF2 captures greater than half the variance (26.9 ± 2.1%) that EOF1 does (48.7 ± 2.6%), whereas the latitude-native EOF2 captures barely a third (19.8 ± 1.0%) of the variance that EOF1 does (56.4 ± 3.5%) The centers of action for the MSAM are shifted equatorward compared to the MNAM, and the negative pole of the MSAM is substantially stronger than its positive pole. The jet-shifted MSAM is nearly identical to its native-latitude counterpart. The main difference between the jet-shifted and native-latitude MSAM

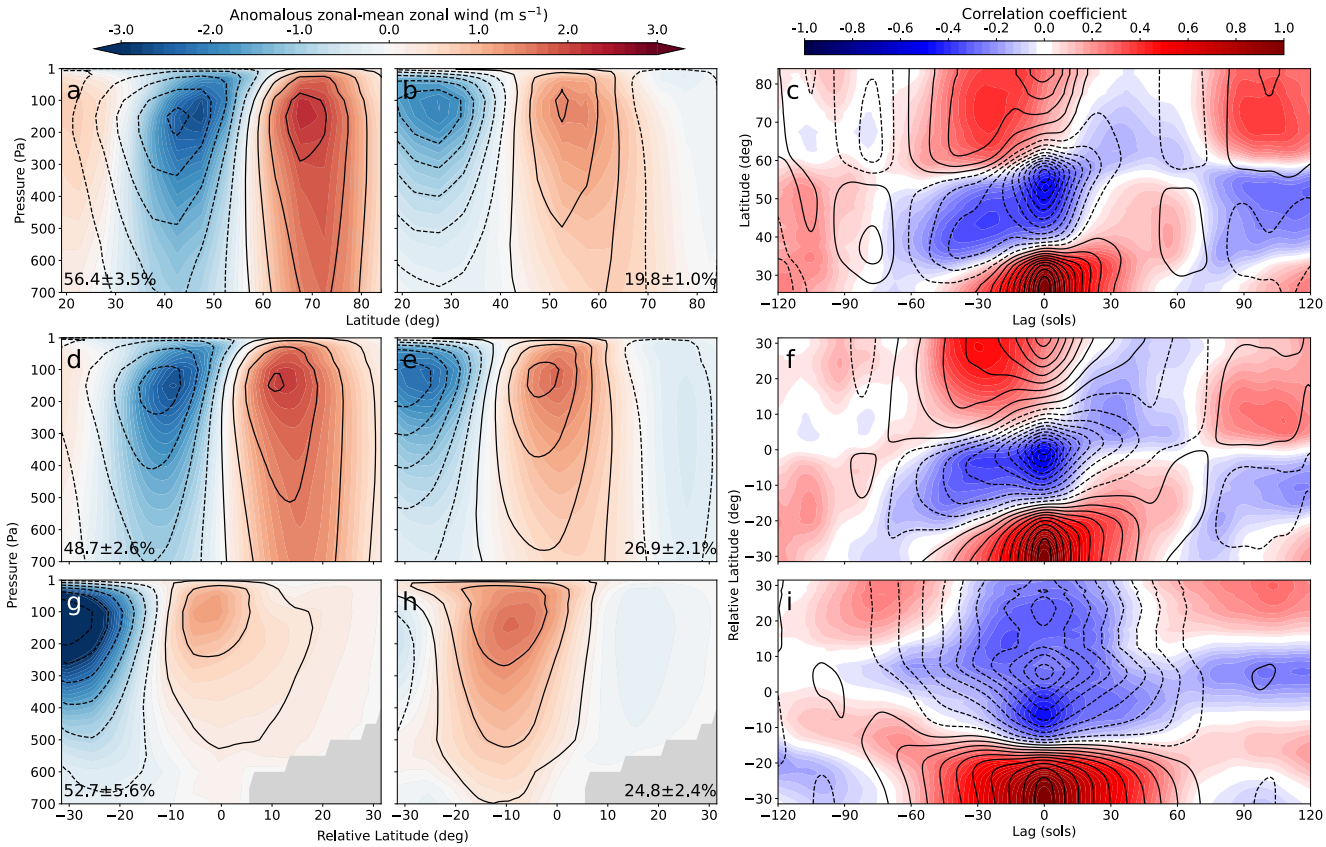

Figure 1. Mars's annular modes as represented in the OpenMARS reanalysis for Mars Years 29–35. Panels a,b,c show Mars's Northern Annular Mode, panels d,e,f show the jet-shifted Northern Annular Mode, and panels g,h,i show the jet-shifted Southern Annular Mode. The left column (panels a, d, g) shows the projection of the climatological anomalous zonal-mean zonal wind back onto EOF1 and the middle column (panels b, e, h) shows the projection onto EOF2. Shading for the left and middle columns indicates projections for each hemisphere's fall–winter, and contours indicate projections for the whole year (contours every 0.25 m s^{-1}). The percent variance explained by each mode with the 95% confidence interval as calculated from the EOF's eigenvalue is shown in each panel. The right column (panels c, f, i) shows the one-point lag-correlation map of the vertically averaged climatologically anomalous zonal-mean zonal wind (shading) and the reconstruction from its projection onto the first two leading EOFs of the climatological anomalous zonal-mean zonal wind (contours every 0.1) with a base latitude of 28°. Only correlations for each hemisphere's fall–winter are shown. Negative relative latitude indicates toward the equator. Light gray shading in panels g,h indicates topography.

versus MNAM is that the jet-shifted eigenvalues for the Southern Hemisphere move further apart (EOF1: 52.7 ± 5.6% and EOF2: 24.8 ± 2.4%) versus the native latitude (EOF1: 51.1 ± 5.1% and EOF2: 25.7 ± 2.3%) rather than closer together, as in the Northern Hemisphere.

3.1. Evidence of Periodic and Propagating Behavior of Mars's Annular Modes

The northern $\langle[\overline{u}]\rangle$ has a clear propagating component as demonstrated in a one-point correlation plot (Figure 1c, shading). The plot is generated by correlating the anomalous $\langle[\overline{u}]\rangle$ timeseries at 28°N to all other latitudes for all lags between ±120 sol during each hemisphere's fall to winter seasons. The correlation point of 28°N is selected to coincide with the negative pole of EOF2. While there is a clear poleward propagation of $\langle[\overline{u}]\rangle$ beginning around 35°N at −75 Mars days (sol), the rate of propagation quickens at positive lag values, with the negative pole reaching 65°N at +40 sol. At lags larger than ±75 sol, the MNAM EOF1 and EOF2 reconstruction has opposite correlation to the full field (Figure 1c, contours). On the other hand, the propagation of the jet-shifted $\langle[\overline{u}]\rangle$ continues at a nearly constant rate from nearly −75 sol at −30° relative latitude to +75 sol +30° relative latitude (Figure 1f, shading). The two-EOF reconstruction better matches the full field at all lags (Figure 1f, contours), indicating that EOF1 and EOF2 are sufficient to capture the propagation of the mode through its full cycle in the jet-shifted latitude coordinate. This demonstrates the importance of the jet shift in describing the propagation.

Conversely, the southern $\langle[\overline{u}]\rangle$ lacks any clear propagation in the native latitude (not shown) or in the jet-shifted coordinate (Figure 1i, shading). The negative pole of correlation has a band that remains within ±10° relative

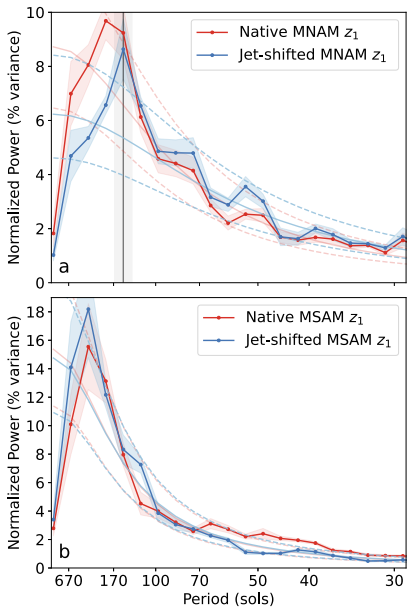

Figure 2. Power spectrum of Mars's annular modes in the Northern (a) and Southern (b) Hemispheres. Solid dark red lines indicate normalized power spectra of the native z_1 zonal index for each mode. Solid dark blue lines indicate power spectra calculated from the jet-shifted z_1 zonal index. Shading indicates the 95% confidence intervals of the power spectra. Light red and blue solid lines indicate the associated red-noise power spectra, with the light red and blue dotted lines indicating the corresponding red-noise 95% confidence intervals. The vertical gray line in panel (a) indicates the only periodicity significantly above red noise, corresponding to the jet-shifted MNAM at ∼146 sol. The width of the light gray bar shows the width of the spectral band.

latitude for ±100 sol of lag. The negative correlation extends to +30° from −10° within ±50 sol of lag, without a third positive center of action that characterizes propagation in the MNAM or Earth's SAM (Lubis & Hassanzadeh, 2021, 2023), leaving only two centers of action. The positive correlation does oscillate somewhat from −30° toward 0° relative latitude at lags greater than ±60 sol; however, this oscillation at such high a period may reflect the incomplete removal of the seasonal cycle, which is stronger in the Southern Hemisphere than the Northern (Figure S1 in Supporting Information S1), and is also considered a reason why idealized model setups for Earth have a more prominent periodicity than reanalyzes (Lubis & Hassanzadeh, 2023). The two-EOF reconstruction matches the full field correlation in the equatorward positive pole, but does not match the timing of the negative pole and is never tripolar in structure. This suggests that, even in the jet-shifted coordinate, the leading two EOFs of the MSAM do not propagate coherently.

We quantify the oscillating nature of the MNAM by calculating the power spectra of the leading principal component, the zonal index (z_1). Of the four spectra calculated for the MNAM and MSAM at native and jet-shifted latitudes, only the jet-shifted z_1 has any power significantly surpassing red noise at any periodicity longer than 50 sol (Figure 2a, gray line). The jet-shifted z_1 has a peak at 146^{+24}_{-14} sol, with the error bars given as the width of the binned power spectrum. The native-latitude z_1 similarly has a peak across 146–195 sol, but this falls within the 95% confidence envelope of red noise. The MSAM spectrum has no peak at ∼150 sol, instead favoring ∼330 sol, which corresponds approximately to half a seasonal cycle, again suggesting contamination of the time series by the seasonal cycle or lingering influence of sporadic large-scale dust events.

Evidence of MNAM propagation is also found in the cross correlation of z_1 and z_2. By construction, the principal components are uncorrelated at lag 0, but they are significantly correlated at other lags (Figure 3a), maximizing at +20 and again at +60 sol at a magnitude of approximately 0.1 and minimizing between −25 and −60 sol at approximately −0.1. This means that after about 20 sol, the EOF2 pattern propagates toward the pole to resemble EOF1, and EOF1 propagates poleward to resemble EOF2. This timescale is somewhat longer than the equivalent shift for Earth of about 7 days despite the periodicity of the oscillation for both Earth and Mars being around 150 days.

Significant positive cross correlations of $z_j m_j$ for $j = 1, 2$ indicate feedback of the anomalous mean flow represented by EOFj on to the eddy momentum fluxes of transient eddies represented by m_j, which then reinforce z_j. The forcing of individual modes (EOF1 or EOF2) on Earth occurs due to positive cross correlations between the zonal wind and eddy momentum flux convergence ($z_1 m_1$ or $z_2 m_2$) just before lag 0, and this also occurs for the MNAM at a lag of −2 sol (Figures 3b and 3c, orange and red). A similar timing for the sign and magnitude is generally true for $z_2 m_2$. The cross correlations of the MSAM are positive for $z_1 m_1$ for lags of −60 to +20 sol and mostly insignificant for $z_2 m_2$ (Figures 3b and 3c, blue); we leave this for future investigation.

Modes on Earth persist in their positive or negative phases due to positive $z_j m_j$ at longer positive lags. For Earth, indications of persistence occur in $z_1 m_1$ at a lag of ∼10 days (Hassanzadeh & Kuang, 2019; Lorenz & Hartmann, 2001; Ma et al., 2017; Simpson et al., 2013), but Mars has positive $z_1 m_1$ out to 25 sol that are significant. A second significant peak in $z_1 m_1$ for the MNAM occurs at ∼60 sol (Figure 3b, red, orange). Conversely, $z_2 m_2$ for Earth is non-existent at larger positive lags, but Mars's $z_2 m_2$ is significantly positive at a lag of 50–60 sol. The reasons for the significant positive $z_j m_j$ out to long lags and the implicated persistence of the leading two MNAM modes at such delayed lags are unclear but may be due to the prevalence of long-period waves (Battalio, 2022; Battalio et al., 2025; Battalio & Wang, 2020; Gong et al., 2023; Wang, 2017).

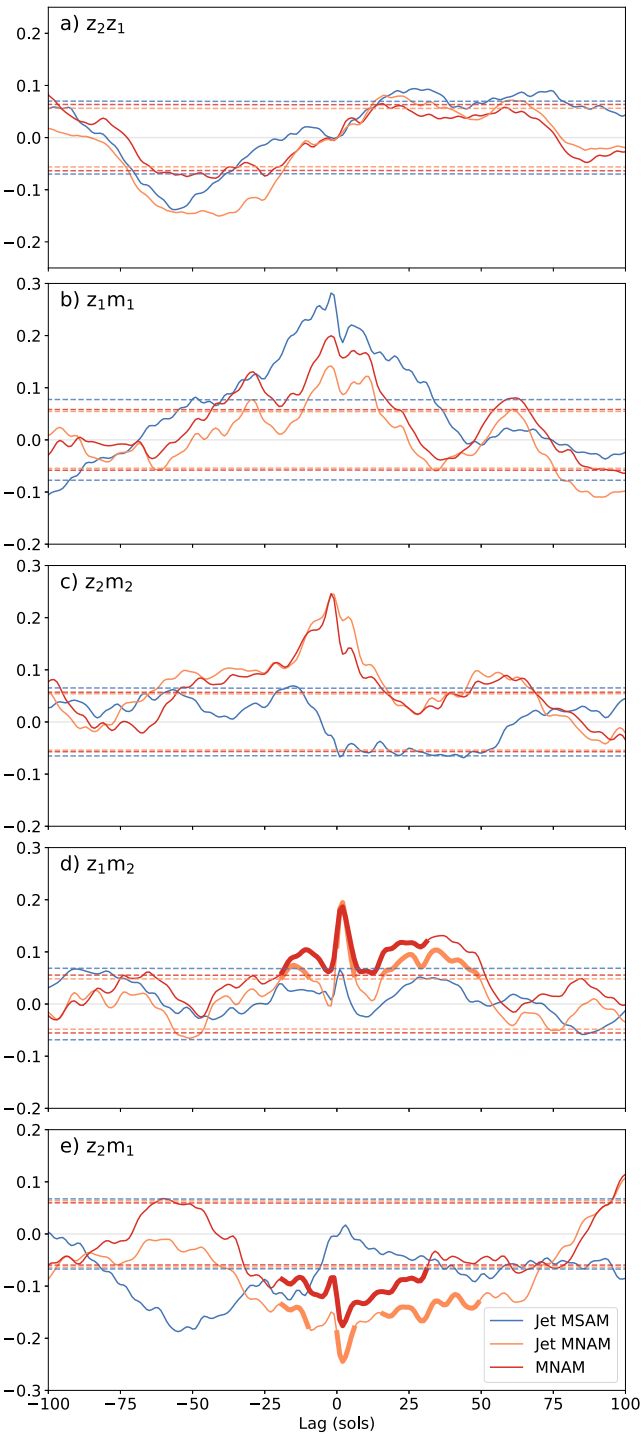

Figure 3. Cross-correlation of the principal component zonal indices of the MNAM (red), jet-shifted MNAM (orange), and jet-shifted MSAM (blue). Shown are the cross correlation of $z_1(t)$ and $z_2(t)$ (a), $z_1(t)$ and $m_1(t)$ (b), $z_2(t)$ and $m_2(t)$ (c), $z_1(t)$ and $m_2(t)$ (d), and $z_2(t)$ and $m_1(t)$ (e). $m_j(t)$ are the eddy momentum forcing indices. Dashed lines represent the 95% confidence interval according to the Bartlett test for each curve, and thick lines in panels d and e indicate significance of z_1m_2 and z_2m_1 at the same lag.

Propagation of EOFs stems from feedback between the modes, which we diagnose as significant cross correlations of z_1m_2 or z_2m_1 (Lubis & Hassanzadeh, 2021, 2023). Here, significant cross correlations of z_1m_2 indicate feedback of EOF1 onto m_2, which modifies EOF1, or vice versa for EOF2. Earth's SAM exhibits significant z_1m_2 and z_2m_1 out to lags of ∼25 days (Lubis & Hassanzadeh, 2021), and the MNAM and MSAM do as well (Figures 3d and 3e). However, the range of positive lags where both z_1m_2 and z_2m_1 are significant is limited to lags of −20–30 sol for the native-latitude MNAM or −20–−8, 0–8, and 20–50 sol for the jet-shifted MNAM (Figures 3d and 3e, thick lines). Neither the native-latitude nor jet-shifted MSAM (Figures 3d and 3e, blue) have significant cross correlations that are significant with opposite signs, similar to a non-propagating regime (Lubis & Hassanzadeh, 2023; Sheshadri & Plumb, 2017). The indication of significant correlations between the EOFs robustly demonstrates cross-EOF feedback, which therefore implicates this feedback in jet stream propagation. To better diagnose the propagation causes, we apply the model of Lubis and Hassanzadeh (2021) to the MNAM and MSAM.

3.2. Reduced-Order Model of Propagation of Mars's Annular Modes

The propagating behavior of the MNAM and the non-propagating regime of the MSAM are captured by the reduced-order model of Lubis and Hassanzadeh (2021); Lubis and Hassanzadeh (2023), which is an extension of the model of Lorenz and Hartmann (2001) to project the zonal momentum equation onto the two leading EOFs of $\langle[\overline{u}]\rangle$ (see Text S2 in Supporting Information S1). In this model, the future states of z_j are predicted from the current z_j and m_j, where $j = 1,2$.

The analytical solution of this model (Text S2 in Supporting Information S1) gives the oscillation frequency

$$\omega = \frac{1}{2}\sqrt{\left[\left(\frac{1}{\tau_1}-\frac{1}{\tau_2}\right)-(b_{11}-b_{22})\right]^2+4b_{12}b_{21}}. \quad (4)$$

The coefficients (b_{jk}) indicate the strength of the cross-EOF feedback; they measure the strength of the feedback of z_j onto z_k. A negative radicand in Equation 4 is a necessary and sufficient condition for propagation. Therefore, $b_{12}b_{21} < 0$ is itself a necessary condition, so cross-EOF feedbacks must be of opposite signs to permit propagation (b_{jk} represent the strength of these feedbacks). We estimate the b_{jk} coefficients from the z_{jk} and m_{jk} time series from OpenMARS using linear regression for lags with significant cross correlations of z_1m_2 and z_2m_1 for positive lags (lags of 12–20 sol), which is similar to the range for Earth (Lubis & Hassanzadeh, 2021, 2023). The timescales (τ_j) are calculated from the e-folding auto-correlation of z_j (Lubis & Hassanzadeh, 2021).

The values for b_{jk} and τ_j for the native and jet-shifted MNAM and MSAM are given in Table S1 (Supporting Information S1). The jet-shifted and native-latitude MSAM possess opposite signed cross-EOF feedbacks, but both have very long oscillatory periods that are not resolvable in a single fall-winter half year. The critical result is that only the jet-shifted MNAM lies in the propagating regime with a frequency of ∼144 sol. This agrees perfectly with the observed periodicity, despite the additional external factors present in Mars's atmosphere compared to Earth's.

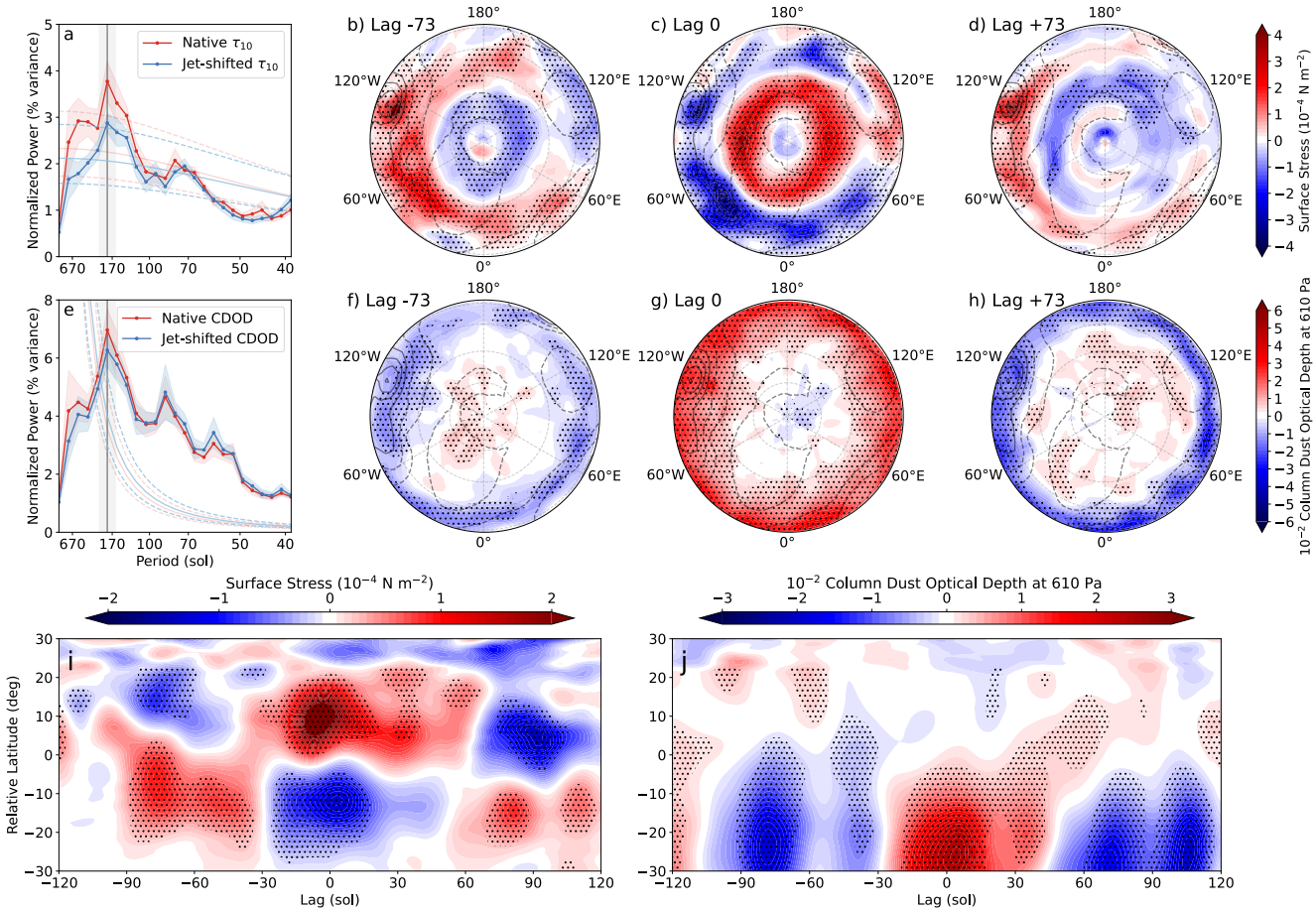

Figure 4. Periodicity of surface wind stress and column dust optical depth (CDOD) in the Northern Hemisphere of Mars. Spectra of the principal components of the native-latitude (red) and jet-shifted (blue) anomalous zonal-mean surface wind stress (a) and CDOD (e) in the OpenMARS reanalysis for MY 29–35. Shading indicates 95% confidence levels, the light solid curve shows the red noise spectrum, and light dotted lines show its 95% confidence interval. The vertical gray line in panel a indicates the only periodicity significantly above red noise of the surface wind stress at ∼175 sol. The width of the light gray bar shows the width of the spectral band. In panel e, the vertical gray line shows the longest period above red noise of the jet-shifted CDOD. Panels b,c,d show lead-lag composites for differences in anomalous, jet-shifted surface wind stress. Panels f,g,h show the same for the anomalous CDOD. Composites are lagged at −73 (b), (f), 0 (c),(g) or +73 (d), (h) sol with respect to extrema in the 140–170-sol filtered z_1 index. Latitude circles are drawn at 75, 60, and 45°. Panels i and j show the lead-lag composites of the zonal-mean anomalous, jet-shifted surface wind stress (i) and CDOD (j). Stippling indicates anomalies at 95% confidence.

3.3. Impact of Annular Mode Propagation on the Dust Cycle

We next investigate whether MNAM propagation impacts the climate of Mars beyond regulating the position of the jet stream with time. In particular, we investigate two possible impacts of the MNAM propagation on Mars's dust cycle. First, a large percentage of dust lifting on Mars is thought to be due directly to straight-line surface wind stress (Kahre et al., 2006), so we investigate whether the surface wind stress is affected by the MNAM propagation. We create a time series of the surface wind stress (Text S1 in Supporting Information S1) by projecting the jet-shifted MNAM EOF1 on the zonally averaged, climatologically anomalous, jet-shifted surface wind stress. A power spectrum of the surface wind stress index highlights the same periodicity (156–187 sol) as the MNAM propagation (Figure 4a, blue). This spectral band is the only periodicity above red noise at periods longer than 30 sol (The spectrum of native-latitude surface wind stress has a broad peak from red noise around 134–187 sol (Figure 4a, red.)

Second, column dust also appears to be affected by the propagation of the MNAM. The power spectrum of an index of the jet-shifted CDOD, calculated in the same way as above, has power above red noise at all periods shorter than ∼180 sol, but has decreasing power that is also below red noise at longer periods (Figure 4e, blue). This cutoff between more or less power than red noise matches the peak period of the surface wind stress. The index of the native-latitude CDOD exhibits a similar cutoff (Figure 4e, red).

The subtle differences between the native latitude and jet-shifted time series at seasonal to yearly timescales suggest that the general circulation, through the Hadley cell, externally generates variability in the midlatitude jet stream. However, at the seasonal timescale of internally driven annular mode propagation, the surface wind stress and CDOD both have annular oscillatory signals. At a lag of −73 sol (one half the 145 sol period of the z_1 index), a composite of the jet-shifted surface wind stress found from extrema of the MNAM (Text S3 in Supporting Information S1) exhibits bands of anomalies (Figure 4b), positive at the northern pole and a relative latitude of 45°, and negative at 65° and 30°. At a lag of 0 sol, the surface wind stress anomalies are at a half oscillation later in the propagation cycle compared to −73 sol and are therefore opposite (Figure 4c). The propagation of the strongest winds results in the northward shift of the negative bands of anomalies from 30° to 45° and 65° to the pole, with the positive anomalies at the pole vanishing and the positive anomalies at 45° shifting to 70°. Similarly, at a lag of +73 sol, the propagation has completed one full cycle, so positive and negative anomaly bands return to the −73 sol lag positions (Figure 4d). This propagation cycle of the anomalous surface stress is shown in Figure 4i over ±120 sol. The propagation is not as smooth as the zonal-mean wind itself, but the dipole pattern clearly flips every ∼75 sol.

Anomalous CDOD does not propagate poleward as obviously but does have a repeating cycle of zonal bands. At a lag of −73 sol, jet-shifted CDOD anomalies are negative equatorward of 45° and positive along 75° (Figure 4f). At a lag of 0 sol, CDOD anomalies are positive equatorward of 45° and more negative toward the pole (Figure 4g). Finally, in completing the cycle at +73 sol lag, the negative anomalies return equatorward of 45° (Figure 4h). This propagation cycle of the anomalous CDOD is shown in Figure 4j over ±120 sol. The propagation of CDOD is only obvious for the positive anomalies at sol 0, but the 150 sol periodicity toward the equator is robust. The cycles shown by the anomalies of the surface wind stress and CDOD and in their power spectra is consistent with the response of Earth's atmosphere to the SAM propagation in the surface wind stress and precipitation (A. G. Marshall et al., 2018; Hell et al., 2021; Lubis & Hassanzadeh, 2023).

Finally, the internal feedbacks of the annular modes with each other have effects on large-scale climate on Mars. The dust cycle on Mars exhibits extreme inter-annual variability due to the non-regular occurrence of global dust events (Battalio et al., 2023; Wang et al., 2023; Wolkenberg et al., 2020). Many global dust events have significant lifting in the Southern Hemisphere. However, most events are initiated as a flushing dust storm from the Northern Hemisphere, so in actuality, Northern Hemisphere oscillations could contribute significantly to global dust event occurrence. The period of MNAM propagation as a non-integer multiple of the year length may contribute to the variability since a favorable phase of the MNAM on the anomalous the surface wind stress might not align with one of the dust event windows encouraged by the seasonal cycle (Kass et al., 2016) every year or for many years at a time. Further, a favorable phase of the 150-sol cycle could possibly occur twice in a given Mars dusty season, which could explain why, in at least one year (1977), two global dust events occurred in a single year (Shirley et al., 2020). We estimate the effect of the MNAM propagation on global dust event incidence by counting the number of peaks that time series with the same power spectrum as the jet-shifted z_1 would have during the historical global dust event season (L_s = 185–310°). Using a Monte Carlo approach on a combined MNAM-insolation metric (Text S4 in Supporting Information S1), we find on average that ∼65.2 ± 2.7% of Mars years would have a unfavorable alignment of the insolation cycle and z_1 for a global dust event, ∼31.1 ± 1.7% of years would have favorable alignment for one event, and ∼3.3 ± 1.1% would have two events. Interestingly, 0.4 ± 0.3% have more than two events. The observed record of global dust events includes a total of 26 Mars years (onward from 1970, inclusive of MY 8–37 but absent MY 13 and 14). Eight years have one global event (31%), one year has two global events (4%), and 17 have no global events (65%) (Shirley et al., 2020). These observed ratios agree with the Monte Carlo experiments. While we do not demonstrate that the MNAM propagation can predict global dust events, the incidence agreement highlights the possibility that interactions of the MNAM and the seasonal cycle may be a contributing factor on the cadence of global dust events and suggests the potential for future predictive capabilities.

4. Summary and Conclusions

We have demonstrated that Mars's northern annular mode (MNAM) in the anomalous zonal-mean zonal wind ($\langle[\overline{u}]\rangle$) has an oscillatory behavior with a period of ∼150 sol. The periodic signal emerges as a result of poleward propagation of the jet stream. This internally forced propagation is embedded within the larger seasonal propagation of the jet stream that is externally forced by the large variation of the outer edge of the Hadley cell. While propagation of the jet stream is evident directly from $\langle[\overline{u}]\rangle$ (Figure 1c), the propagating signal is more robust when

the seasonal cycle is removed (Figure 1f). Consistently, the power spectra of the principal components of the leading modes of variability of the latitude-shifted $\langle[\overline{u}]\rangle$ are significantly above red noise only at a period of ∼150 sol in the Northern Hemisphere. This MNAM propagation period can be reproduced using a reduced-order model (Lubis & Hassanzadeh, 2021, 2023), which indicates that propagation is due to the feedback between eddy momentum flux convergence associated with the first and second leading EOFs of $\langle[\overline{u}]\rangle$.

We have also found that the period of oscillation that emerges from MNAM propagation is reflected in the surface wind stress and column dust optical depth in the northern hemisphere (Figure 4). The modulation of wind stress by the MNAM, with a frequency separate from the seasonal cycle, may thus contribute to the observed extreme interannual variability of regional and global dust events, as suggested by our estimate of the relative frequency of favorable phasing of the annular mode and insolation cycle. Continued monitoring of the Martian climate or modeling studies may enable testing of this possibility.

Future work should examine the factors that enable propagation of the MNAM but prevent it for the MSAM. Also, propagation of the Earth's SAM might be related to the quasi-biennial oscillation (Kuroda & Yamazaki, 2010; Roscoe & Haigh, 2007), yet the fact that at least one of Mars's annular modes propagates despite the lack of a Martian quasi-biennial oscillation (Battalio, 2025) presents a question for the mechanisms linking the two phenomena. Finally, the propagation timescale on Mars and Earth is similar. This may be due to their nearly equal planetary rotation rates imbuing similar timescales into the baroclinic wave lifecycles and the eddy momentum flux divergence that feeds back onto zonal wind. Future modeling efforts will be required to pinpoint the exact cause of the timescale similarity.

Data Availability Statement

The OpenMARS reanalysis is available at (Holmes et al., 2024). The column dust optical depth dataset is available at (Montabone, Millour, et al., 2020).

Acknowledgments
JMB and JML are supported by NASA Mars Data Analysis Program Grant 80NSSC21K1095. SL is supported by the Office of Science, U.S. Department of Energy Biological and Environmental Research as part of the Regional and Global Climate Model Analysis program area. PH received support from NSF grant AGS-2046309. We extend the utmost appreciation to two anonymous reviewers for their comments that greatly improved the paper.

References

Barnes, J. R., Haberle, R. M., Wilson, R. J., Lewis, S. R., Murphy, J. R., & Read, P. L. (2017). The global circulation. In R. M. Haberle, R. T. Clancy, F. Forget, M. D. Smith, & R. W. E. Zurek (Eds.), *The atmosphere and climate of Mars* (pp. 229–294). Cambridge University Press. https://doi.org/10.1017/9781139060172.009

Battalio, J. M. (2022). Transient eddy kinetic energetics on Mars in three reanalysis datasets. *Journal of the Atmospheric Sciences*, *79*(2), 361–382. https://doi.org/10.1175/JAS-D-21-0038.1

Battalio, J. M. (2025). Quasi-Biennial Oscillation absent in Mars atmospheric reanalysis datasets. *Icarus*, *427*, 116367. https://doi.org/10.1016/j.icarus.2024.116367

Battalio, J. M., Cohen, M. J., Read, P. L., Lora, J. M., McConnochie, T. H., & McGouldrick, K. (2025). Oscillations in terrestrial planetary atmospheres. In *Atmospheric oscillations* (pp. 399–441). Elsevier. https://doi.org/10.1016/B978-0-443-15638-0.00019-8

Battalio, J. M., & Lora, J. M. (2021). Annular modes of variability in the atmospheres of Mars and Titan. *Nature Astronomy*, *5*(11), 1139–1147. https://doi.org/10.1038/s41550-021-01447-4

Battalio, J. M., & Wang, H. (2020). Eddy evolution during large dust storms. *Icarus*, *338*, 113507. (October 2019). https://doi.org/10.1016/j.icarus.2019.113507

Battalio, J. M., & Wang, H. (2021). The Mars dust activity database (MDAD): A comprehensive statistical study of dust storm sequences. *Icarus*, *354*, 114059. (August 2020). https://doi.org/10.1016/j.icarus.2020.114059

Battalio, J. M., Wang, H., Richardson, M. I., Toigo, A. D., & Saidel, M. (2023). Spatial extent of dust storm boundaries in the Mars dust activity database. *Icarus*, *400*, 115567. https://doi.org/10.1016/j.icarus.2023.115567

Butler, A. H., Thompson, D. W., & Gurney, K. R. (2007). Observed relationships between the Southern Annular Mode and atmospheric carbon dioxide. *Global Biogeochemical Cycles*, *21*(4), 1–8. https://doi.org/10.1029/2006GB002796

Chung, C., & Nigam, S. (1999). Weighting of geophysical data in principal component analysis. *Journal of Geophysical Research*, *104*(D14), 16925–16928. https://doi.org/10.1029/1999jd900234

Doddridge, E. W., & Marshall, J. (2017). Modulation of the seasonal cycle of antarctic sea ice extent related to the southern annular mode. *Geophysical Research Letters*, *44*(19), 9761–9768. https://doi.org/10.1002/2017GL074319

Eabry, M. D., Goyal, R., Taschetto, A. S., Hobbs, W., & Gupta, A. S. (2024). Combined impacts of southern annular mode and zonal wave 3 on Antarctic Sea ice variability. *Journal of Climate*, *37*(5), 1759–1775. https://doi.org/10.1175/JCLI-D-23-0516.1

Feldstein, S., & Lee, S. (1998). Is the atmospheric zonal index driven by an eddy feedback? *Journal of the Atmospheric Sciences*, *55*(19), 3077–3086. https://doi.org/10.1175/1520-0469(1998)055⟨3077:ITAZID⟩2.0.CO;2

Feldstein, S. B. (2000). The timescale, power spectra, and climate noise properties of teleconnection patterns. *Journal of Climate*, *13*(24), 4430–4440. https://doi.org/10.1175/1520-0442(2000)013⟨4430:TTPSAC⟩2.0.CO;2

Gong, Y., Xiao, Q., Ma, Z., Zhang, S., Zhou, Q., Huang, C., & Huang, K. (2023). A unique vertical structure of quasi-20-sol waves observed by the MCS on the martian atmosphere. *Journal of Geophysical Research: Space Physics*, *128*(10), e2023JA031605. https://doi.org/10.1029/2023JA031605

Guendelman, I., & Kaspi, Y. (2022). The key factors controlling the seasonality of planetary climate. *AGU Advances*, *3*(5). https://doi.org/10.1029/2022AV000684

Hannachi, A., Jolliffe, I. T., & Stephenson, D. B. (2007). Empirical orthogonal functions and related techniques in atmospheric science: A review. *International Journal of Climatology*, *27*(9), 1119–1152. https://doi.org/10.1002/joc

Hartmann, D. L., & Lo, F. (1998). Wave-driven zonal flow vacillation in the Southern Hemisphere. *Journal of the Atmospheric Sciences*, *55*(8), 1303–1315. https://doi.org/10.1175/1520-0469(1998)055⟨1303:WDZFVI⟩2.0.CO;2

Hassanzadeh, P., & Kuang, Z. (2019). Quantifying the annular mode dynamics in an idealized atmosphere. *Journal of the Atmospheric Sciences*, *76*(4), 1107–1124. https://doi.org/10.1175/jas-d-18-0268.1

Hell, M. C., Cornuelle, B. D., Gille, S. T., & Lutsko, N. J. (2021). Time-varying empirical probability densities of southern ocean surface winds: Linking the leading mode to SAM and quantifying wind product differences. *Journal of Climate*, *34*(13), 5497–5522. https://doi.org/10.1175/JCLI-D-20-0629.1

Holmes, J., Lewis, S., & Patel, M. (2024). OpenMARS database (version 5). The Open University Collection. [Dataset]. https://doi.org/10.21954/ou.rd.c.4278950

Holmes, J. A., Lewis, S. R., & Patel, M. R. (2020). OpenMARS: A global record of martian weather from 1999-2015. *Planetary and Space Science*, *188*, 104962. (September 2019). https://doi.org/10.1016/j.pss.2020.104962

Kahre, M. A., Murphy, J. R., & Haberle, R. M. (2006). Modelling the Martian dust cycle and surface dust reservoirs with the NASA Ames general circulation model. *Journal of Geophysical Research E: Planets*, *111*(6), 1–25. https://doi.org/10.1029/2005JE002588

Kahre, M. A., Murphy, J. R., Haberle, R. M., Montmessin, F., & Schaeffer, J. (2005). Simulating the Martian dust cycle with a finite surface dust reservoir. *Geophysical Research Letters*, *32*(20). https://doi.org/10.1029/2005GL023495

Kass, D. M., Kleinböhl, A., McCleese, D. J., Schofield, J. T., & Smith, M. D. (2016). Interannual similarity in the Martian atmosphere during the dust storm season. *Geophysical Research Letters*, *43*(12), 6111–6118. (May). https://doi.org/10.1002/2016GL068978

Kidson, J. W. (1988). Interannual variations in the southern hemisphere circulation. *Journal of Climate*, *1*(12), 1177–1198. https://doi.org/10.1175/1520-0442(1988)001⟨1177:IVITSH⟩2.0.CO;2

Kuroda, Y., & Yamazaki, K. (2010). Influence of the solar cycle and QBO modulation on the southern annular mode. *Geophysical Research Letters*, *37*(12). https://doi.org/10.1029/2010GL043252

Lorenz, D. J., & Hartmann, D. L. (2001). Eddy-zonal flow feedback in the southern hemisphere. *Journal of the Atmospheric Sciences*, *58*(21), 3312–3327. https://doi.org/10.1175/1520-0469(2001)058,3312:EZFFIT.2.0.CO;2

Lu, J., Harrop, B. E., Lubis, S. W., Smith, S., Chen, G., & Leung, L. R. (2024). The role of cloud radiative effects in the propagating southern annular mode. *Journal of Geophysical Research: Atmospheres*, *129*(8), e2023JD040428. https://doi.org/10.1029/2023JD040428

Lubis, S. W., & Hassanzadeh, P. (2021). An eddy-zonal flow feedback model for propagating annular modes. *Journal of the Atmospheric Sciences*, *78*(1), 249–267. https://doi.org/10.1175/JAS-D-20-0214.1

Lubis, S. W., & Hassanzadeh, P. (2023). The intrinsic 150-day periodicity of the southern hemisphere extratropical large-scale atmospheric circulation. *AGU Advances*, *4*(3), e2022AV000833. https://doi.org/10.1029/2022AV000833

Ma, D., Hassanzadeh, P., & Kuang, Z. (2017). Quantifying the eddy–jet feedback strength of the annular mode in an idealized GCM and reanalysis data. *Journal of the Atmospheric Sciences*, *74*(2), 393–407. https://doi.org/10.1175/JAS-D-16-0157.1

Marshall, A. G., Hemer, M. A., Hendon, H. H., & McInnes, K. L. (2018). Southern annular mode impacts on global ocean surface waves. *Ocean Modelling*, *129*, 58–74. https://doi.org/10.1016/j.ocemod.2018.07.007

Marshall, G. J., Thompson, D. W., & van den Broeke, M. R. (2017). The signature of southern hemisphere atmospheric circulation patterns in Antarctic precipitation. *Geophysical Research Letters*, *44*(22), 11580–11589. https://doi.org/10.1002/2017GL075998

Montabone, L., Forget, F., Millour, E., Wilson, R. J., Lewis, S. R., Cantor, B. A., et al. (2015). Eight-year climatology of dust optical depth on Mars. *Icarus*, *251*, 65–95. https://doi.org/10.1016/j.icarus.2014.12.034

Montabone, L., Millour, E., Forget, F., Spiga, A., Kass, D., & Kleinböhl, A. (2020). Martian year 34 climatology of the atmospheric column dust optical depth. *ESPRI/IPSL*. [Dataset]. https://doi.org/10.14768/20191217001.1

Montabone, L., Spiga, A., Kass, D. M., Kleinböhl, A., Forget, F., & Millour, E. (2020). Martian year 34 column dust climatology from Mars climate sounder observations: Reconstructed maps and model simulations. *Journal of Geophysical Research: Planets*, *125*(8). https://doi.org/10.1029/2019JE006111

Newman, C. E., & Richardson, M. I. (2015). The impact of surface dust source exhaustion on the martian dust cycle, dust storms and interannual variability, as simulated by the MarsWRF General Circulation Model. *Icarus*, *257*, 47–87. https://doi.org/10.1016/j.icarus.2015.03.030

Read, P. L., Lewis, S. R., & Mulholland, D. P. (2015). The physics of martian weather and climate: A review. *Reports on Progress in Physics*, *78*(12), 125901. https://doi.org/10.1088/0034-4885/78/12/125901

Roscoe, H. K., & Haigh, J. D. (2007). Influences of ozone depletion, the solar cycle and the QBO on the Southern Annular Mode. *Quarterly Journal of the Royal Meteorological Society*, *133*(628), 1855–1864. https://doi.org/10.1002/qj.153

Sheshadri, A., & Plumb, R. A. (2017). Propagating annular modes: Empirical orthogonal functions, principal oscillation patterns, and time scales. *Journal of the Atmospheric Sciences*, *74*(5), 1345–1361. https://doi.org/10.1175/JAS-D-16-0291.1

Shirley, J. H. (2015). Solar System dynamics and global-scale dust storms on Mars. *Icarus*, *251*, 128–144. https://doi.org/10.1016/j.icarus.2014.09.038

Shirley, J. H., McKim, R. J., Battalio, J. M., & Kass, D. M. (2020). Orbit-spin coupling and the triggering of the martian planet-encircling dust storm of 2018. *Journal of Geophysical Research: Planets*, *125*(6), 1–39. https://doi.org/10.1029/2019je006077

Simpson, I. R., Shepherd, T. G., Hitchcock, P., & Scinocca, J. F. (2013). Southern annular mode dynamics in observations and models. Part II: Eddy feedbacks. *Journal of Climate*, *26*(14), 5220–5241. https://doi.org/10.1175/JCLI-D-12-00495.1

Son, S.-W., & Lee, S. (2006). Preferred modes of variability and their relationship with climate change. *Journal of Climate*, *19*(10), 2063–2075. https://doi.org/10.1175/JCLI3705.1

Thompson, D. W., & Wallace, J. M. (2000). Annular modes in the extratropical circulation. Part I: Month-to-month variability. *Journal of Climate*, *13*(5), 1000–1016. https://doi.org/10.1175/1520-0442(2000)013⟨1000:AMITEC⟩2.0.CO;2

Thompson, D. W. J., & Barnes, E. A. (2014). Periodic variability in the large-scale southern hemisphere atmospheric circulation. *Science*, *343*(6171), 641–645. (February). https://doi.org/10.1126/science.1247660

Wang, H. (2017). Major dust storms and westward traveling waves on Mars. *Geophysical Research Letters*, *44*(8), 3493–3501. https://doi.org/10.1002/2017GL072894

Wang, H., Saidel, M., Richardson, M. I., Toigo, A. D., & Battalio, J. M. (2023). Martian dust storm distribution and annual cycle from Mars daily global map observations. *Icarus*, *394*, 115416. https://doi.org/10.1016/j.icarus.2022.115416

Williams, R. S., Marshall, G. J., Levine, X., Graff, L. S., Handorf, D., Johnston, N. M., et al. (2024). Future Antarctic climate: Storylines of midlatitude jet strengthening and shift emergent from CMIP6. *Journal of Climate*, *37*(7), 2157–2178. https://doi.org/10.1175/JCLI-D-23-0122.1

Wolkenberg, P., Giuranna, M., Smith, M. D., Grassi, D., & Amoroso, M. (2020). Similarities and differences of global dust storms in MY 25, 28, and 34. *Journal of Geophysical Research: Planets*, *125*(3), 1–16. https://doi.org/10.1029/2019JE006104

References From the Supporting Information

Forget, F., Hourdin, F., Fournier, R., Hourdin, C., Talagrand, O., Collins, M., et al. (1999). Improved general circulation models of the Martian atmosphere from the surface to above 80 km. *Journal of Geophysical Research*, *104*(E10), 24155–24175. https://doi.org/10.1029/1999JE001025

Kleinböhl, A., Schofield, J. T., Kass, D. M., Abdou, W. A., Backus, C. R., Sen, B., et al. (2009). Mars Climate Sounder limb profile retrieval of atmospheric temperature, pressure, and dust and water ice opacity. *Journal of Geophysical Research E: Planets*, *114*(10), 1–30. https://doi.org/10.1029/2009JE003358

Lewis, S. R., Read, P. L., Conrath, B. J., Pearl, J. C., & Smith, M. D. (2007). Assimilation of thermal emission spectrometer atmospheric data during the Mars Global Surveyor aerobraking period. *Icarus*, *192*(2), 327–347. https://doi.org/10.1016/j.icarus.2007.08.009

May, R. M., Goebbert, K. H., Thielen, J. E., Leeman, J. R., Camron, M. D., Bruick, Z., et al. (2022). MetPy: A meteorological Python library for data analysis and visualization. *Bulletin of the American Meteorological Society*, *103*(10), E2273–E2284. https://doi.org/10.1175/BAMS-D-21-0125.1